15 Mar 2022

An Accurate and Computationally Efficient Method for Battery Capacity Fade Modeling

D. M. Ajiboye

Jonathan W. Kimball
Missouri University of Science and Technology, kimballjw@mst.edu

R.(Robert) G. Landers
Missouri University of Science and Technology, landersr@mst.edu

John (T.) Park
Missouri University of Science and Technology, parkj@mst.edu

Recommended Citation

D. M. Ajiboye et al., "An Accurate and Computationally Efficient Method for Battery Capacity Fade Modeling," *Chemical Engineering Journal*, vol. 432, article no. 134342, Elsevier, Mar 2022.
The definitive version is available at https://doi.org/10.1016/j.cej.2021.134342

Chemical Engineering Journal 432 (2022) 134342

Contents lists available at ScienceDirect

Chemical Engineering Journal

journal homepage: www.elsevier.com/locate/cej

An accurate and computationally efficient method for battery capacity fade modeling

D.M. Ajiboye [a], J.W. Kimball [b], R.G. Landers [c], J. Park [a,*]

[a] Department of Mechanical and Aerospace Engineering, Missouri University of Science and Technology, Rolla, MO 65409, USA
[b] Department of Electrical and Computer Engineering, Missouri University of Science and Technology, Rolla, MO 65409, USA
[c] Department of Aerospace and Mechanical Engineering, University of Notre Dame, South Bend, IN 46556, USA

ARTICLE INFO

Keywords:
Battery capacity fade modeling
Chebyshev spectral method

ABSTRACT

The industry demand for accurate and fast algorithms that model vital battery parameters, e.g., state-of-health, state-of-charge, pulse-power capability, is substantial. One of the most critical models is battery capacity fade. The key challenge with physics-based battery capacity fade modeling is the high numerical cost in solving complex models. In this study, an efficient and fast model is presented to capture capacity fade in lithium-ion batteries. Here, the high-order Chebyshev spectral method is employed to address the associated complexity with physics-based capacity fade models. Its many advantages, such as low computational memory, high accuracy, exponential convergence, and ease of implementation, allow us to efficiently model a comprehensive array of degradation physics such as solid electrolyte interface film formation, hydrogen evolution, manganese deposition, salt decomposition, manganese dissolution, and electrolyte oxidation. In this work, we developed a modeling framework that accurately and efficiently predicted degradation in a lithium-ion battery over extended cycles. For example, in long cycle battery operation, the implemented Chebyshev spectral method algorithm was found to be within 0.1358% – 0.28% of a high-fidelity model, while simulation times were reduced by an average of 91%. The developed Chebyshev spectral method algorithm shows great potential in advanced battery management systems, where maintaining accuracy and achieving a fast response is critical.

1. Introduction

Lithium-ion batteries (LIBs) are ubiquitous in modern day applications (e.g., electric vehicles, portable devices, stationary applications). Their immense market penetration is due to their high energy density, high power density, and comparatively low cost. Despite these excellent properties, their usage is hampered by rapid capacity fade, poor cyclability, and instability, especially at high temperatures. These deficiencies demand an effective tool for monitoring their status (e.g., state-of-health (SOH), state-of-charge (SOC), remaining useful life (RUL), and state-of-power (SOP)) during operation.

A BMS consists of hardware and software tools that collaboratively control the charging and discharging of a battery pack, in order to ensure its reliable and safe operation [1]. To ensure safety, the BMS must prevent the battery pack from overcharging and reaching high temperatures [2]. Furthermore, BMSs also perform cell balancing and fault detection functions in battery packs. To carry out these functions, advanced BMSs monitor battery pack states, and estimate such quantities as SOH, SOC, RUL, and SOP. Considering these parameters are unmeasurable, appropriate models are typically used. The commonly employed models are classified into two groups: equivalent circuit models (ECMs) [3–6] and physics-based electrochemical models (PEMs). In ECMs, electrical-circuit analogs are employed to simulate the cell voltage response to different current profiles. Although ECMs are simpler and easier to implement than PEMs, they lack high fidelity and offer limited information on a battery's inherent status. In comparison, PEMs, like the pseudo-two-dimensional model (P2D)—simulate the behavior of a battery by relating the reaction kinetics and species (i.e., ions and electrons) transport to current and voltage [7,8]. Its advantage lies in its dependence on the inherent physics of a battery, thereby enhancing accuracy. Despite its accuracy, widespread use of this model is limited in BMS applications due to its associated computational cost and complexity. The inclusion of degradation physics to PEMs for SOH purposes will make this issue worse.

The viability of computational tools in improving the efficiency and life-cycle of LIBs were previously discussed in [9,10]. For example, Smith et al. [11] showed that a 50% increase in the useful power density

* Corresponding author.
E-mail address: parkjonghy@mst.edu (J. Park).

https://doi.org/10.1016/j.cej.2021.134342
Received 21 October 2021; Received in revised form 8 December 2021; Accepted 21 December 2021
Available online 28 December 2021

Nomenclature

c_1	Solid phase concentration $[mol{\cdot}m^{-3}]$
c_2	Solution phase concentration $[mol{\cdot}m^{-3}]$
c_{H^+}	Concentration of H^+ species $[mol{\cdot}m^{-3}]$
$c_{Mn^{2+}}$	Concentration of Mn^{2+} species $[mol{\cdot}m^{-3}]$
c_{H_2O}	Concentration of water $[mol{\cdot}m^{-3}]$
c_1^{max}	Maximum solid phase concentration $[mol{\cdot}m^{-3}]$
c_1^{surf}	Solid phase surface concentration $[mol{\cdot}m^{-3}]$
D_1	Solid phase diffusion coefficient $[m^2{\cdot}s^{-1}]$
D_2	Solution phase diffusion coefficient $[m^2{\cdot}s^{-1}]$
$D_{H^+}^{eff}$	Effective diffusivity of H^+ $[m^2{\cdot}s^{-1}]$
$D_{Mn^{2+}}^{eff}$	Effective diffusivity of Mn^{2+} $[m^2{\cdot}s^{-1}]$
$D_{H_2O}^{eff}$	Effective diffusivity of H_2O $[m^2{\cdot}s^{-1}]$
$D_2^{eff} = D_2{\cdot}\varepsilon_2^{brugg}$	Effective solution phase diffusion coefficient $[m^2{\cdot}s^{-1}]$
F	Faraday's constant $[C{\cdot}mol^{-1}]$
I_{app}	Applied current density $[A{\cdot}m^{-2}]$
i_0	Exchange current density $[m^2{\cdot}s^{-1}]$
$j_{loc,i}$	Local intercalation current $[mol{\cdot}\ m^{-2}{\cdot}s^{-1}]$
$keff_i = k_2(c_2){\cdot}\varepsilon_i^{brugg}$	Effective solution phase ionic conductivity $[S{\cdot}m^{-1}]$
$k_{junc} = \frac{2RT}{F}(1-t_+^0)$	Junction potential pre-factor.
R	Gas constant $[J{\cdot}mol^{-1}{\cdot}K^{-1}]$
S_i	Specific surface area of active materials $[m^{-1}]$
U_{ocp}	Open circuit potential $[V]$

Greek letters

φ_1	Solid phase potential $[V]$
φ_2	Solution phase potential $[V]$
η_{oxid}	Overpotential for oxidation side reaction $[V]$
ε_2	Electrolyte volume fraction
σ_i^{eff}	Effective solid phase electronic conductivity $[S{\cdot}m^{-1}]$
η_i	Overpotential $[V]$
δ_{SEI}	SEI layer thickness $[m]$
$\theta_i = \frac{c_1^{surf}}{c_1^{max}}$	Normalized surface concentration

Superscripts

eff	*effective*
max	*maximum*
surf	*surface*
pos	*positive*

Subscripts

ocp	open circuit potential
app	applied
a	*anode electrode*
c	*cathode electrode*
s	*separator*
oxid	*oxidation*
dis	*dissolution*
dep	*deposition*

Abbreviations

LIBs	Lithium-ion batteries
SOH	State-of-health
SOC	State-of-charge
RUL	Remaining useful life
SOP	State-of-power
ECMs	Equivalent circuit models
PEMs	Physics-based electrochemical models
P2D	Pseudo-two-dimensional model
BMSs	Battery management systems
CSM	Chebyshev spectral method
SEI	Solid electrolyte interphase
EC	Ethylene carbonate
FEM	Finite element method
FDM	Finite difference method
DAE	Differential-algebraic equation
IDAS	Implicit differential–algebraic equation solver with sensitivity capabilities
SUNDIALS	Suite of nonlinear and differential/algebraic equation solvers
BDF	Backward differentiation Formula
RMSE	Root-mean-square-error

of LIBs can be achieved via physics-based battery health management systems. Rahimian et al. [12] used physics-based dynamic optimization techniques to extend the useful life of a cell by 29.28%. In addition, Lin et al. [13] employed optimization methods in a physics-based battery model to extend battery life cycle by 200%, after 100 cycles. In these examples, the employed methods differed from traditional approaches because they used physics-based battery control algorithms [9] to extend battery life-cycle. In contrast, traditional methods simply impose strict safety limits [9] on battery parameters, e.g., current, SOC, and temperature. Overall, modeling is essential to, understanding behavior, design, discovery, estimation and control of lithium-ion batteries [14]. In order to achieve the aforementioned gains, the current state-of-the-art actively incorporates physics-based modeling into Battery Management Systems (BMSs) [2,15,16].

Another important aspect is the computational efficiency. In the literature, several modeling techniques have been developed to efficiently model and reduce the associated complexity with physics-based battery models. For example, Northrop et al. [17] used coordinate transformation, orthogonal collocation and reformulation techniques to efficiently simulate battery stack models. Bizeray et al. [8] employed Chebyshev orthogonal collocation techniques in conjunction with an extended Kalman filter algorithm, to estimate the states in a battery model. Using asymptotic techniques, Planella et al. [18] systematically derived a fast and accurate thermal single particle model with electrolyte dynamics. In these prior battery modeling works, the associated capacity fade mechanisms in lithium-ion batteries were ostensibly omitted. This is because inclusion of these mechanisms will significantly increase the complexity of the modeling process.

In this work, an advanced mathematical model is developed and implemented to capture the capacity fade in a battery accurately and efficiently. The model employs the Chebyshev spectral method (CSM) [7,8,19], which is known for its accuracy, ease of implementation, exponential convergence and reduced computational cost. The capacity fade model considers solid-electrolyte interface film formation, Mn deposition, and hydrogen evolution [20] as the dominant degradation mechanisms in the anode electrode. In the cathode domain, manganese dissolution, electrolyte oxidation, and salt decomposition are modeled as the fundamental degradation mechanisms [20–22]. In addition to the side reactions in the electrodes, salt decomposition in all of the domains (i.e., anode, separator, and cathode) was also modeled. These degradation mechanisms are primarily modeled with mass and charge conservation equations in the physics-based P2D battery modeling framework. The implemented capacity fade model consists of 5 partial differential equations, 5 ordinary differential equations, and 7 algebraic

equations. Our implementation of this capacity fade model, using the CSM demonstrates its potential for use in an advanced battery management system. Finally, the numerically implemented capacity fade model was computationally validated using COMSOL Multiphysics® and sundialsTB solvers.

2. Modeling section

2.1. Capacity fade model

In the implemented capacity fade model, we consider $Li_yMn_2O_4$/Li_xC_6 battery chemistry, as a demonstration. The modeled side reactions in the anode are solid electrolyte interphase (SEI) film formation, Mn deposition, and H_2 evolution [20]. In the cathode domain, the considered degradation mechanisms are localized Mn dissolution, electrolyte oxidation, and salt decomposition [20]. The cathodic side reactions were coupled such that solvent/electrolyte oxidation and salt decomposition play an active role in Mn dissolution. All these degradation mechanisms were modeled using side reactions expressed by appropriate kinetic equations.

The formation of SEI in the anode domain occurs due to a reaction between the lithiated graphite and the electrolyte solvent. This reaction is given by [23]

$$S + 2Li^+ + 2e^- \rightarrow P \tag{1}$$

where S is the solvent (ethylene carbonate (EC) in this work) and P represents the collection of products (ethylene dicarbonate ($CH_2OCO_2Li)_2$ is assumed here) formed due to this side reaction. The adverse effects of SEI formation are in the form of losses in cyclable lithium-ions and increase in anode electrode resistance. In tandem with SEI formation in the anode electrode, manganese deposition and hydrogen evolution also occur. The manganese deposition reaction occurs due to a reduction reaction, as expressed in [20]. Note that the deposition reaction in the anode is a by-product of the manganese dissolution reaction in the cathode. Similar to the formation of the SEI layer, the adverse impact of Mn deposition reaction comes in the form of loss of cyclable lithium-ions. This deposition reaction is given by

$$Mn^{2+} + 2e^- \rightarrow \quad Mn_{(s)} \tag{2}$$

Also, the hydrogen evolution reaction emanates from the protons generated due to electrolyte oxidation and salt decomposition reaction in the cathode domain. The generation and consumption of the protons on the anode surface is [20]

$$H^+ + e^- \rightarrow \frac{1}{2}H_{2(g)} \tag{3}$$

In the cathode domain also, multiple degradation mechanisms are considered, this includes manganese dissolution, salt decomposition, and solvent oxidation. The solvent oxidation reaction in the cathode is [21,24]

$$Solvent \xrightarrow{oxidation} Sl_o + H^+ + e^- \tag{4}$$

where Sl_o describes the solvent oxidation products. The salt decomposition reactions occur due to the reaction of $LiPF_6$ with water in the electrolyte. This reaction is

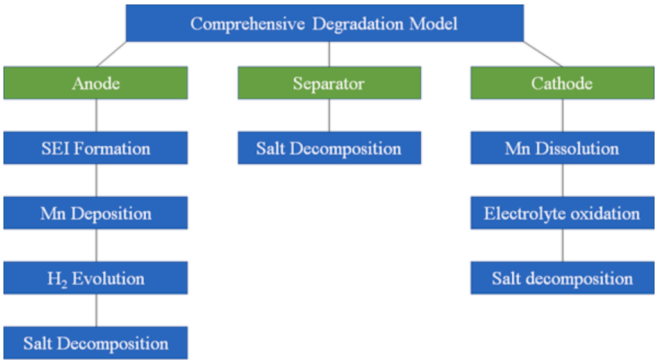

Fig. 1. Schematic showing the modeled degradation mechanisms [11–13,17].

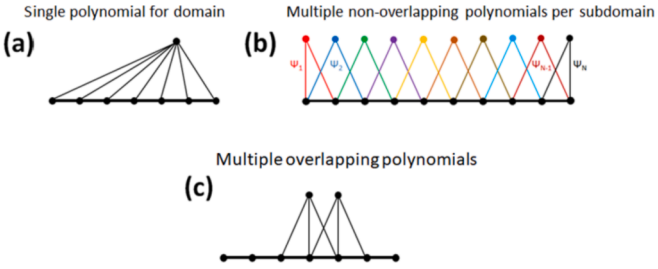

Fig. 2. Comparison of discretization methods. (a) Chebyshev spectral method (b) Finite element method and (c) Finite difference method [26,29].

$$LiPF_6 \xrightarrow{oxidation} LiF + PF_5 \tag{5}$$

where PF_5 subsequently reacts with water to form HF acid. The acid attack induced Mn dissolution in the cathode domain is expressed by the following chemical reaction [20,25]

$$4H^+ + 2LiMn_2O_4 \rightarrow 2Li^+ + Mn^{2+} + \frac{3}{2}Mn_2O_4 + 2H_2O \tag{6}$$

Here, it is assumed that a fraction of Mn^{2+} precipitates to form MnF_2 composite on the cathode surface. The degradation mechanisms, shown schematically in Fig. 1, were implemented in the physics-based P2D model in the form of side-reactions. All of the required governing and capacity fade equations are given in Appendix A.

2.2. Chebyshev spectral method implementation of the comprehensive capacity fade model

To discretize the governing equations in the capacity fade model, the CSM is employed. This method is chosen specifically because of its computational efficiency, exponential convergence, low-memory requirement [26–28], and high accuracy. Compared to traditional methods, like the finite element method (FEM) and the finite difference method (FDM), the CSM employs global basis functions with higher

order polynomials defined over the whole (see Fig. 2a with the schematic representation of the global basis function and discretization nodes) computational domain [26–28]. Whereas, in the case of the FEM, the computational domain is discretized into sub-intervals, where the approximating polynomials are nonzero over a couple of sub-intervals (see Fig. 2b). In the FEM, three fundamental approaches are employed for improving accuracy: h-refinement, r-refinement, and p-refinement. For the FDM, the unknown function is approximated using a sequence of multiple overlapping low-order polynomials (see Fig. 2c).

The first step in the CSM method involves transformation of the problem domain into the interval [−1, 1], using a non-uniform distribution that has been shown to be more accurate [28,30] than its uniform counterpart. This distribution is the Chebyshev Gauss-Lobatto points defined as,

$$z_p = -cos\left(\frac{p\pi}{N}\right) \qquad p = 0, \ldots N \tag{7}$$

Given a grid function $u_p = u(z_p)$, where $p = 0, \ldots N$ and N is the number of subintervals, the approximation polynomial $u^{(N)}(z)$ is

$$u^{(N)}(z) = \sum_{p=0}^{N} u_p l_p^N(z) \tag{8}$$

where $l_p^N(z)$ is the Lagrange polynomial

$$l_p^N(z) = \prod_{j=0, j\neq p}^{N} \frac{z - z_j}{z_p - z_j} \qquad p, j = 0, \ldots, N \tag{9}$$

The $(N + 1)$ nodal values of u_p are

$$U = (u_0, \ldots, u_N)^t \tag{10}$$

$$U^{(k)} = \left(u_0^{(k)} \equiv \frac{d^k u^{(N)}}{dz^k}\bigg|_{z_0}, \ldots, u_p^{(k)} \equiv \frac{d^k u^{(N)}}{dz^k}\bigg|_{z_p}, \ldots, u_N^{(k)} \equiv \frac{d^k u^{(N)}}{dz^k}\bigg|_{z_N}\right)^t \tag{11}$$

where k is an integer representing the differentiation order. The discrete differentiation matrix for the differential operators, is then defined by the expression $D_{GL}^k U = U^{(k)}$ [28],

$$D_{GL} = \begin{bmatrix} -\frac{2N^2+1}{6} & \cdots & -\frac{(-1)^N}{2} \\ \vdots & \ddots & \vdots \\ \frac{\overline{c}_i}{\overline{c}_j}\frac{(-1)^{i+j}}{(z_i - z_j)} & \cdots & \frac{-z_j}{2\left(1 - z_j^2\right)} \\ \vdots & \ddots & \vdots \\ \frac{(-1)^N}{2} & \cdots & \frac{2N^2+1}{6} \end{bmatrix} \tag{12}$$

where

$$\overline{c}_n = \begin{cases} 2 & n = 0 \quad or \quad n = N \\ 1 & 1 \leqslant n \leqslant N-1 \end{cases} \tag{13}$$

This differentiation matrix is valid for the Cartesian coordinate system over the Gauss-Lobatto grid points. For equations in the spherical coordinate system whose second derivative operator are singular at the center i.e., at $r = 0$, a non-uniform Chebyshev grid called the Gauss-Radau is used. The differentiation matrix using the Gauss-Radau grid has only one boundary point i.e., $r = R$, and the other boundary is defined to be close to $r = 0$ but never on it. The Gauss-Radau grid points are then defined as,

$$x_p = -cos\left(\frac{(2p+1)\pi}{2L+1}\right), \qquad p = 0, \ldots, L \tag{14}$$

Given the Gauss-Radau points, the appropriate approximation polynomial is

$$u_p = \sum_{n=0}^{L} \widehat{u}_n T_n(x_p), \qquad p = 0, \ldots, L \tag{15}$$

where

$$T_n(x_p) = (-1)^n cos\left(\frac{(2p+1)n\pi}{2L+1}\right) \tag{16}$$

and $\widehat{u}_n$ is the Gauss-Radau pseudo spectrum of $u^{(N)}(z)$ and it is expressed as

$$\widehat{u}_n = \frac{2}{N\overline{c}_n} \sum_{p=0}^{N} \frac{1}{\overline{c}_p} T_n(z_p) u_p, \qquad n = 0, \ldots, N \tag{17}$$

To derive the differentiation matrix for the Gauss-Radau grid points, the Gauss-Radau transformation matrix T_{GR} and its inverse were used

$$(T_{GR})_{np} = (-1)^n cos\left(\frac{(2p+1)n\pi}{2L+1}\right), \qquad n, p = 0, \ldots, L \tag{18}$$

$$\left(T_{GR}^{-1}\right)_{np} = \frac{4(-1)^n}{(2L+1)c_n c_{L-p}}(-1)^n cos\left(\frac{(2p+1)n\pi}{2L+1}\right), \qquad n, p = 0, \ldots, L \tag{19}$$

The Gauss-Radau differentiation matrix is

$$D_{GR} = T_{GR} \cdot \widehat{D} \cdot T_{GR}^{-1} \tag{20}$$

where $\widehat{D}$ is the pseudo-spectral differentiation matrix, and it is

$$\widehat{D} = \left(T^{-1}\right)_{np} \cdot D_{GL} \cdot T_{pn}, \qquad n, p = 0, \ldots, L \tag{21}$$

The matrices T_{pn} and $\left(T^{-1}\right)_{np}$, respectively, are

$$T_{pn} = (-1)^n cos\left(pn\frac{\pi}{N}\right), \qquad n, p = 0, \ldots, N \tag{22}$$

$$\left(T^{-1}\right)_{pn} = \frac{2(-1)^n}{N\overline{c}_n\overline{c}_p} cos\left(np\frac{\pi}{N}\right), \qquad n, p = 0, \ldots, N \tag{23}$$

where

$$\overline{c}_p = \begin{cases} 2 & p = 0 \quad or \quad p = N \\ 1 & 1 \leqslant p \leqslant N-1 \end{cases} \tag{24}$$

For illustrative purposes, we show the implementation of the CSM for the solid phase concentration equation given as [20,21],

$$\frac{\partial c_1}{\partial t} = D_{1,i}\frac{1}{r^2}\frac{\partial}{\partial r}\left(r^2\frac{\partial c_1}{\partial r}\right) \tag{25}$$

$$D_{1,i}\left.\frac{\partial c_1}{\partial r}\right|_{r=0} = 0 \tag{26}$$

$$D_{1,i}\left.\frac{\partial c_1}{\partial r}\right|_{r=R_a} = \frac{-j_{Li,i}}{F} \tag{27}$$

As a first step, the solid phase concentration equation is normalized using the following relationships: $\bar{r} = r/R$, $r^2 = \bar{r}^2R^2$ and $\partial/\partial r = 1/R{\cdot}\partial/\partial\bar{r}$. These relationships transform Eq. (25) into

$$\frac{\partial c_1}{\partial t} = \frac{1}{\bar{r}^2R^3}\frac{\partial}{\partial\bar{r}}\left[D_1\bar{r}^2R\frac{\partial c_1}{\partial\bar{r}}\right] \tag{28}$$

Multiplication of Eq. (28) by $\bar{r}^2R$ gives

$$\bar{r}^2R\frac{\partial c_1}{\partial t} = \frac{\partial}{\partial\bar{r}}\left[D_1\frac{\bar{r}^2}{R}\frac{\partial c_1}{\partial\bar{r}}\right] \tag{29}$$

Eq. (29) is rewritten as

$$\bar{r}^2R\frac{\partial c_1}{\partial t} = \frac{2\bar{r}}{R}D_1\frac{\partial c_1}{\partial\bar{r}} + D_1\frac{\bar{r}^2}{R}\frac{\partial^2 c_1}{\partial\bar{r}^2} \tag{30}$$

The radial derivative in Eq. (30) is transformed to the Cartesian coordinate using $x = 2\bar{r}/R - 1$. This gives the following relationships,

$$\frac{\partial c_1}{\partial\bar{r}} = x_{\bar{r}}\frac{\partial c_1}{\partial x} = \frac{2}{R}\frac{\partial c_1}{\partial x} \tag{31}$$

$$\frac{\partial^2 c_1}{\partial\bar{r}^2} = (x_{\bar{r}}c_x)_x x_{\bar{r}} = \frac{4}{R^2}\frac{\partial^2 c_1}{\partial x^2} \tag{32}$$

The radial points in Eq. (30) is transformed to the Cartesian coordinate using $\bar{r} = \frac{1+x_p}{2}$. Use of Eqs. (31)–(32) in Eq. (30) gives,

$$\left(\frac{x_p+1}{2}\right)^2 R\frac{\partial c_1}{\partial t} = \frac{2}{R}\left(\frac{x_p+1}{2}\right)2D_1\frac{\partial c_1}{\partial x} + \frac{4D_1}{R}\left(\frac{x_p+1}{2}\right)^2\frac{\partial^2 c_1}{\partial x^2} \tag{33}$$

and the boundary condition at $r = R$ gives,

$$D_1\left.\frac{\partial c_1}{\partial r}\right|_{r=R} = \frac{2D_1}{R}\left.\frac{\partial c_1}{\partial x}\right|_{x_p=1} \tag{34}$$

In explicit terms, the solid phase concentration equation is implemented as

$$\left(\frac{x_p+1}{2}\right)^2 R\frac{\partial c_1}{\partial t} = \frac{2D_1}{R}\left(\frac{x_p+1}{2}\right)^2 2[D_{GR}]\{c_1\} + \frac{D_1}{R}\left(\frac{x_p+1}{2}\right)^2 4\left[D_{GR}^2\right]\{c_1\} \tag{35}$$

$$\left.\frac{2D_1}{R}[D_{GR}]\{c_1\}\right|_{x_p=1} = \frac{-j_{Li,i}}{F} \tag{36}$$

where $[D_{GR}]$ is the Gauss-Radau differentiation matrix, and $\{c_1\}$ is the column vector of unknowns.

Also, we show the implementation of the CSM for the solution phase concentration equation [20],

$$\varepsilon_{2,a}{\cdot}\frac{\partial c_2}{\partial t} = D_a^{eff}\frac{\partial^2 c_2}{\partial x^2} + \frac{1-t^+}{F}S_a{\cdot}j_{loc,a} \tag{37}$$

$$\varepsilon_{2,s}{\cdot}\frac{\partial c_2}{\partial t} = D_s^{eff}\frac{\partial^2 c_2}{\partial x^2} \tag{38}$$

$$\varepsilon_{2,c}\frac{\partial c_2}{\partial t} = D_c^{eff}\frac{\partial^2 c_2}{\partial x^2} + \frac{(1-t^+){\cdot}S_c}{F}j_{loc,c} + \frac{(2S_c{\cdot}i_{Mn\_react} - j_{oxid}{\cdot}a_c)}{F} \tag{39}$$

It is transformed to the unit interval $\bar{x} \in [0,\ \ 1]$ using normalization relationships, and this gives,

$$L_a{\cdot}\varepsilon_{2,a}{\cdot}\frac{\partial c_2}{\partial t} = \frac{D_a^{eff}}{L_a}\frac{\partial^2 c_2}{\partial\bar{x}^2} + \frac{1-t^+}{F}S_a{\cdot}L_a{\cdot}j_{loc,a} \tag{40}$$

$$L_s{\cdot}\varepsilon_{2,s}{\cdot}\frac{\partial c_2}{\partial t} = \frac{D_s^{eff}}{L_s}\frac{\partial^2 c_2}{\partial\bar{x}^2} \tag{41}$$

$$L_c{\cdot}\varepsilon_{2,c}\frac{\partial c_2}{\partial t} = \frac{D_c^{eff}}{L_c}\frac{\partial^2 c_2}{\partial\bar{x}^2} + \frac{(1-t^+){\cdot}S_c}{F}L_c{\cdot}j_{loc,c} + \frac{L_c{\cdot}(2S_c{\cdot}i_{Mn\_react} - j_{oxid}{\cdot}a_c)}{F} \tag{42}$$

Then, Eqs. (40)–(42) are transformed from the unit interval $\bar{x} \in [0, 1]$ to the Chebyshev closed interval $z \in [-1,\ \ 1]$, using the following relationships: $z = 2\bar{x} - 1$, $u_{\bar{x}} = z_{\bar{x}}{\cdot}u_z = 2{\cdot}u_z$, $u_{\bar{x}\bar{x}} = (z_{\bar{x}}{\cdot}u_z)z_{\bar{x}} = 4{\cdot}u_{zz}$. This gives,

$$L_a{\cdot}\varepsilon_{2,a}{\cdot}\frac{\partial c_2}{\partial t} = \frac{4D_a^{eff}}{L_a}\left[D_{GL}^2\right]\{c_2\} + \frac{1-t^+}{F}S_a{\cdot}L_a{\cdot}j_{loc,a} \tag{43}$$

$$L_s{\cdot}\varepsilon_{2,s}{\cdot}\frac{\partial c_2}{\partial t} = \frac{4D_s^{eff}}{L_s}\left[D_{GL}^2\right]\{c_2\} \tag{44}$$

$$L_c{\cdot}\varepsilon_{2,c}\frac{\partial c_2}{\partial t} = \frac{4D_c^{eff}}{L_c}\left[D_{GL}^2\right]\{c_2\} + \frac{(1-t^+){\cdot}S_i}{F}L_c{\cdot}j_{loc,c} + \frac{L_c{\cdot}(2S_c{\cdot}i_{Mn\_react} - j_{oxid}{\cdot}a_c)}{F} \tag{45}$$

where $[D_{GL}]$ is the Gauss-Lobatto differentiation matrix, and $\{c_2\}$ is the column vector of unknowns. The same normalization approach is applied to all of the other governing equations in the capacity fade model. The equations in the capacity fade model constitutes a nonlinear differential–algebraic equation (DAE) system, and require consistent initialization due to its inherent stiffness [31]. The initialization routine is implemented for the algebraic variables (i.e., φ_1, φ_2, and $j_{loc,a}$) using the fsolve command in MATLAB®. In a state-space form, the nonlinear DAE system is expressed as,

$$\begin{cases} M\dfrac{\partial y}{\partial t} = f(t, y_1, y_2) \\ 0 = g(t, y_1, y_2) \end{cases} \tag{46}$$

where $y_1 = [c_1,\ \ c_2,\ \ c_{H^+},\ \ c_{Mn^{2+}}, c_{H_2O},\ \ \delta_{SEI},\ \ \varepsilon_1,\ \ \varepsilon_{us}]$, $y_2 = [\varphi_1, \varphi_2,\ \ j_{loc,a}]$ and M is the time-dependent mass matrix. In an expanded format, Eq. (46) is given as,

$$
\begin{bmatrix}
\left(\frac{x_p+1}{2}\right)^2 R_i & & & & & & & & & & & \\
& L_i\cdot\varepsilon_2 & & & & & & & & & & \\
& & L_i\cdot\varepsilon_2 & & & & & & & & & \\
& & & L_i\cdot\varepsilon_2 & & & & & & & & \\
& & & & L_i\cdot\varepsilon_2 & & & & & & & \\
& & & & & L_i\cdot\varepsilon_2 & & & & & & \\
& & & & & & 1 & & & & & \\
& & & & & & & 1 & & & & \\
& & & & & & & & 1 & & & \\
& & & & & & & & & 0 & & \\
& & & & & & & & & & 0 & \\
& & & & & & & & & & & 0
\end{bmatrix}
\begin{Bmatrix}
\dot{c}_1 \\ \dot{c}_2 \\ \dot{c}_{H^+} \\ \dot{c}_{Mn^{2+}} \\ \dot{c}_{H_2O} \\ \dot{\delta}_{SEI} \\ \dot{\varepsilon}_2 \\ \dot{\varepsilon}_{us} \\ \dot{\varphi}_1 \\ \dot{\varphi}_2 \\ j_{loc,a}
\end{Bmatrix} =
$$

$$
\begin{bmatrix}
\frac{2D_1}{R}\left(\frac{x_p+1}{2}\right)2\cdot[D_{GR}]+\frac{D_1}{R}\left(\frac{x_p+1}{2}\right)^2 4\cdot[D_{GR}^2] & & & & & & & & & & & \\
& \frac{4D_2^{eff}}{L_i}\cdot[D_{GL}^2] & & & & & & & & & & \\
& & \frac{4D_{H^+}^{eff}}{L_i}\cdot[D_{GL}^2] & & & & & & & & & \\
& & & \frac{4D_{Mn^{2+}}^{eff}}{L_i}\cdot[D_{GL}^2] & & & & & & & & \\
& & & & \frac{4D_{H_2O}^{eff}}{L_i}\cdot[D_{GL}^2] & & & & & & & \\
& & & & & 0 & & & & & & \\
& & & & & & 0 & & & & & \\
& & & & & & & 0 & & & & \\
& & & & & & & & \frac{4\sigma_i^{eff}}{L_i}\cdot[D_{GL}^2] & & & \\
\frac{4k_{junc}}{L_i\cdot c_2}[D_{GL}]\cdot\{keff_i\}\cdot[D_{GL}]+\frac{4keff_i}{L_i}\frac{k_{junc}}{c_2}\cdot[D_{GL}^2] & & & & & & & & & -\frac{4}{L_i}\cdot[D_{GL}]\{keff_i\}\cdot[D_{GL}]-\frac{4keff_i}{L_i}\cdot[D_{GL}^2] & & \\
& & & & & & & & & & & 1
\end{bmatrix}
\begin{Bmatrix}
c_1 \\ c_2 \\ c_{H^+} \\ c_{Mn^{2+}} \\ c_{H_2O} \\ \delta_{SEI} \\ \varepsilon_2 \\ \varepsilon_{us} \\ \varphi_1 \\ \varphi_2 \\ j_{loc,a}
\end{Bmatrix}
+
\begin{Bmatrix}
0 \\ f_{c_2}\cdot L_i \\ f_{c_{H^+}}\cdot L_i \\ f_{c_{Mn^{2+}}}\cdot L_i \\ f_{c_{H_2O}}\cdot L_i \\ f_{\delta_{SEI}} \\ f_{\varepsilon_2} \\ f_{\varepsilon_{us}} \\ -f_{\varphi_1}\cdot L_i \\ -f_{\varphi_2}\cdot L_i-\frac{2k_{junc}\cdot keff_i}{L_i\cdot c_2}([D_{GL}]\{c_2\})^2 \\ -f_{j_{loc,a}}
\end{Bmatrix}
\tag{47}
$$

where f_{c_2}, $f_{c_{H^+}}$, $f_{c_{Mn^{2+}}}$, $f_{c_{H_2O}}$, $f_{\delta_{SEI}}$, f_{ε_2}, $f_{\varepsilon_{us}}$, f_{φ_1}, f_{φ_2}, $f_{\varepsilon_{us}}$, $f_{j_{loc,a}}$ are the source terms from the listed governing equations in Appendix A.

Upon discretization using the CSM, the time dependent differential equations become ordinary differential equations, while the non-time dependent differential equations adopt algebraic states. For the integration of the arising system of DAE given in Eq. (47), the ode15s solver in MATLAB® is used. Also, to improve the rate of convergence in the model, we linearize the nonlinear source terms using a Taylor series expansion. Another objective of linearization is to improve the implicitness of the model [29], such that the source terms are implemented at a time step closer to the $(n+1)$ iteration. The use of linearization techniques for the nonlinear source terms is valid because at the point of convergence, $\varphi^{(n+1)} = \varphi^{(n)}$. In scientific computations, [29,32], the general rule of thumb is to implement linearization only for cases where the left hand side diagonals are strengthened. In this capacity fade model, this rule of thumb applies only to the solution phase potential equation. Also, we assume that the diffusion dynamics (i.e., c_1, c_2, c_{H^+}, $c_{Mn^{2+}}$, c_{H_2O}) in the model are significantly slower than the electrical potentials (i.e., φ_1 *and* φ_2). This assumption allows the equilibrium potentials and solution conductivities to be considered constant when solving the algebraic equations [33]. The combination of this assumption and the linearization rule of thumb leads to the quasi-linearization of the solution phase potential equation. Application of the Taylor series linearization technique on the nonlinear source terms generally takes the following form [29],

$$
j_{loc,i}^{(n+1)} = j_{loc,i}^{(n)} + \left.\frac{dj_{loc,i}}{d\varphi_2}\right|^{(n)} \left(\varphi_2^{(n+1)} - \varphi_2^{(n)}\right) \tag{48}
$$

For illustration purposes, we show the linearization of the solution phase potential equation expressed as,

$$
\frac{\partial}{\partial x}\left[-keff_i\left(\frac{\partial\varphi_2}{\partial x}-\frac{k_{junc}}{c_2}\frac{\partial c_2}{\partial x}\right)\right] = j_{loc,i}\cdot S_i \qquad i = a, \quad c \tag{49}
$$

where its nonlinear source terms in the anode and cathode are given as,

$$
j_{loc,a} = i_0\left\{exp\left[\frac{\alpha_a F}{RT}\left(\eta_i - R_{SEI}\cdot j_{loc,a}\right)\right] - exp\left[\frac{-\alpha_c F}{RT}\left(\eta_i - R_{SEI}\cdot j_{loc,a}\right)\right]\right\} \tag{50}
$$

$$
j_{loc,c} = i_0\left\{exp\left[\frac{\alpha_a F}{RT}\eta_i\right] - exp\left[\frac{-\alpha_c F}{RT}\eta_i\right]\right\} \tag{51}
$$

Application of Eq. (48) on the anode source term gives the following derivative expression

Table 1
Battery model parameters used for the numerical studies in this paper [20].

Parameters	Anode	Separator	Cathode
Initial solid phase concentration c_1^0, $[mol \cdot m^{-3}]$	14,870	–	3900
Maximum solid phase concentration c_1^{max}, $[mol \cdot m^{-3}]$	26,390	–	22,860
Initial solution phase concentration c_2^0, $[mol \cdot m^{-3}]$	1000	1000	1000
Solid phase diffusion coefficient D_1, $[m^2 \cdot s^{-1}]$	3.9E-14	–	1E-13
Solution phase diffusion coefficient D_2, $[m^2 \cdot s^{-1}]$	7.5E-11	7.5E-11	7.5E-11
Electrode thickness L_i, $[\mu m]$	100	30	110
Electrode particles' radii R_i, $[\mu m]$	12.5	–	8.5
Solid phase conductivity σ_i, $[S \cdot m^{-1}]$	100	–	3.8
Solid phase volume fraction ε_s	0.471	–	0.297
Solution phase volume fraction (Porosity)ε_2	0.357	1	0.444
Charge transfer coefficient α_i	0.5	–	0.5
Initial solid phase potential φ_1^0, $[V]$	0	–	4.2
Initial solution phase potential φ_2^0, $[V]$	0	0	0
Initial state of charge θ	0.5635	–	0.1706
Cell cross-sectional area A, $[m^2]$	24e-4		
Bruggeman coefficient *brugg*	1.5		
Applied current density I_{app}, $[A \cdot m^{-2}]$	17.5		
Faraday's constant, $[C \cdot mol^{-1}]$	96,487		
Reaction rate coefficient k_0, $[m^{2.5} \cdot mol^{-0.5} \cdot s^{-1}]$	2E-6		
Reaction rate coefficient k_0, $[m^{2.5} \cdot mol^{-0.5} \cdot s^{-1}]$	2E-6		
Universal gas constant R, $[J \cdot mol^{-1} \cdot K^{-1}]$	8.314		
Temperature T, $[K]$	298		
Transference number t_+^0	0.363		
Cut-off voltage $V_{cut-off}$, $[V]$	3.5		
Nominal voltage $[V]$	3.7		
Nominal capacity $[Ah]$	17.5		
Anode material	Graphite		
Cathode material	$Li_yMn_2O_4$ (LMO)		
Electrolyte	$LiPF_6$		
Side Reaction Parameters			
Parameters	Value		
Solvent concentration c_{EC}, $[mol \cdot m^{-3}]$	4541		
Effective diffusivity of H^+ $D_{H^+}^{eff}$, $[m^2 \cdot s^{-1}]$	10E-11 $\cdot \varepsilon_2^p$		
Effective diffusivity of Mn^{2+} $D_{Mn^{2+}}^{eff}$, $[m^2 \cdot s^{-1}]$	5E-11 $\cdot \varepsilon_2^p$		
Effective diffusivity of H_2O $D_{H_2O}^{eff}$, $[m^2 \cdot s^{-1}]$	3E-11 $\cdot \varepsilon_2^p$		
Fraction coefficient of proton generation f_{H^+}	15%		
Fractional coefficient for Mn^{2+} dissolution f_{Mn_dis}	40%		
Reaction rate coefficient for SEI k_{SEI}, $[m \cdot s^{-1}]$	6E-10		
Reaction rate for acid attack k_{dis}, $[m \cdot s^{-1}]$	2E-9		
Reaction rate of Mn deposition k_{Mn_dep}, $[m \cdot s^{-1}]$	80E-9		
Salt decomposition coefficient k_{decom}, $[m^6 \cdot mol^{-2}]$	7.13E-10		
Reaction rate constant for H_2 generation k_{H_2}	2.07E-8		
SEI resistivity k_{res}, $[\Omega \cdot m]$	3E4		
Isolated volume fraction coefficient k_{iso}	8		
Molecular weight of SEI M_{SEI}, $[kg \cdot mol^{-1}]$	0.162		
Equilibrium potential of solvent oxidation U_{oxid}^{eq}, $[V]$	4.1		
Molar volume of $Li_yMn_2O_4$ $\overline{V}$, $[m^3 \cdot mol^{-1}]$	1.4E-4		
Carbon content X_c	10%		
Measured carbon content for a preset value X_c^{ref}	10%		

Table 1 (*continued*)

Parameters	Anode	Separator	Cathode
Cathode charge transfer coefficient for H_2 $\alpha_C^{H_2}$	0.5		
Anodic coefficient for solvent oxidation α_a^{sol}	0.5		
Cathodic coefficient for Mn deposition $\alpha_c^{Mn\_dep}$	0.5		
Cathode charge transfer coefficient for SEI α_C^{SEI}	0.5		
SEI limiting coefficient λ_{SEI}, $[m^{-1}]$	1.2E7		
Mn deposition limiting coefficient λ_{Mn_dep}	3E6		
Limiting coefficient for H_2 generation λ_{H_2}	2E5		
Density of SEI ρ_{SEI}, $[kg \cdot m^{-3}]$	1690		

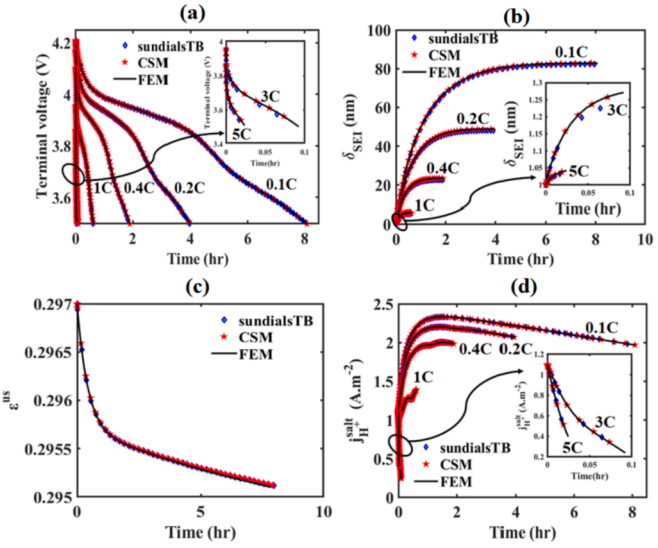

Fig. 3. Analysis of the capacity fade model variables after 1 cycle. (a) Terminal voltage time histories with respect to C-rates, and numerical solvers (CSM with ode15s, CSM with sundialsTB and FEM). (b) Evolution of SEI thickness at $\times = L_a$ for constant discharge using different C rates and numerical solvers. (c) Evolution of usable volume fraction at $\times = L_a + L_s + L_c$ for $I_{app} = 0.1$C using various numerical solvers. (d) Comparison of salt decomposition rate at $x = L_a + L_s + L_c$ for constant-current discharge with different C-rates and numerical solvers.

Table 2
Comparison of voltage RMSE values between CSM using ode15s and sundialsTB.

C-rate	RMSE (mV)	
	CSM with ode15s	CSM with sundialsTB
0.1	0.5583	0.5129
0.2	0.2676	1.019
0.4	0.4952	2.0919
0.6	0.7921	2.8383
0.8	0.8329	3.4885
1	0.8688	3.0852
2	1.1883	5.9186
3	1.5467	6.6493
5	2.6925	6.0415

$$\left.\frac{dj_{loc,a}}{d\varphi_2}\right|^{(n)} = -i_0 \cdot \left(\frac{F \cdot \alpha_a exp\left(\frac{F \cdot \alpha_a \cdot (U_{ocp} - \varphi_1 + \varphi_2 + R_{SEI} \cdot j_{loc,a})}{R \cdot T}\right)}{RT} + \frac{F \cdot \alpha_c exp\left(\frac{F \cdot \alpha_c (U_{ocp} - \varphi_1 + \varphi_2 + R_{SEI} \cdot j_{loc,a})}{R \cdot T}\right)}{RT} \right) \tag{52}$$

then the solution phase potential equation in the anode electrode then takes the following form

$$\left[-\frac{k_i^{eff}}{L_a}\cdot\left[D_{GL}^2\right]+S_a\cdot i_0\cdot L_a\cdot\left(\frac{F\cdot\alpha_a exp\left(\frac{F\cdot\alpha_a\cdot(U_{ocp}-\varphi_1+\varphi_2+R_{SEI}\cdot j_{loc,a})}{R\cdot T}\right)}{RT}+\frac{F\cdot\alpha_c exp\left(\frac{F\cdot\alpha_c(U_{ocp}-\varphi_1+\varphi_2+R_{SEI}\cdot j_{loc,a})}{R\cdot T}\right)}{RT}\right)\right]\varphi_2^{(n+1)}$$
$$=S_a\cdot L_a\cdot j_{loc,a}+S_a\cdot i_0\cdot L_a\cdot\left(\frac{F\cdot\alpha_a exp\left(\frac{\alpha_a\cdot F\cdot(\varphi_1-\varphi_2-U_{ocp})}{R\cdot T}\right)}{RT}+\frac{F\cdot\alpha_c exp\left(\frac{-\alpha_c\cdot F\cdot(\varphi_1-\varphi_2-U_{ocp})}{R\cdot T}\right)}{RT}\right)\varphi_2^{(n)}$$
$$-k_i^{eff}\cdot\frac{k_{junc}}{L_a\cdot c_2}\left[D_{GL}^2\right]\{c_2\} \tag{53}$$

In the case of the cathode electrode, the derivative term from Eq. (48) is expressed as,

$$\left.\frac{dj_{loc,c}}{d\varphi_2}\right|^{(n)}=-i_0\cdot\left(\frac{F\cdot\alpha_a exp\left(\frac{F\cdot\alpha_a\cdot(\varphi_1-\varphi_2-U_{ocp})}{R\cdot T}\right)}{RT}+\frac{F\cdot\alpha_c exp\left(\frac{-F\cdot\alpha_c\cdot(\varphi_1-\varphi_2-U_{ocp})}{R\cdot T}\right)}{RT}\right) \tag{54}$$

where the solution phase potential equation (i.e., Eq. (49)) in the cathode electrode then takes the following form,

$$\left[-\frac{k_i^{eff}}{L_c}\cdot\left[D_{GL}^2\right]+S_c\cdot L_c\cdot\left(\frac{i_0\cdot F\cdot\alpha_a exp\left(\frac{F\cdot\alpha_a\cdot(\varphi_1-\varphi_2-U_{ocp})}{R\cdot T}\right)}{RT}+\frac{i_0\cdot F\cdot\alpha_c exp\left(\frac{-F\cdot\alpha_c\cdot(\varphi_1-\varphi_2-U_{ocp})}{R\cdot T}\right)}{RT}\right)\right]\varphi_2^{(n+1)}$$
$$=S_c\cdot L_c\cdot j_{loc,c}+S_c\cdot L_c\cdot i_0\cdot\left(\frac{F\cdot\alpha_a exp\left(\frac{\alpha_a\cdot F\cdot(\varphi_1-\varphi_2-U_{ocp})}{R\cdot T}\right)}{RT}+\frac{F\cdot\alpha_c exp\left(\frac{-\alpha_c\cdot F\cdot(\varphi_1-\varphi_2-U_{ocp})}{R\cdot T}\right)}{RT}\right)\varphi_2^{(n)}$$
$$-k_i^{eff}\cdot\frac{k_{junc}}{c_2\cdot L_c}\left[D_{GL}^2\right]\{c_2\} \tag{55}$$

Table 3
Comparison of SEI RMSE values between CSM using ode15s and sundialsTB.

C-rate	RMSE (nm)	
	CSM with ode15s	CSM with sundialsTB
0.1	0.1565	0.313
0.2	0.1114	0.5077
0.4	0.11	0.336
0.6	0.0584	0.3767
0.8	0.036	0.1735
1	0.0209	0.1659
2	0.0041	0.0505
3	0.0011	0.0112
5	0.0001	0.0016

Table 4
RMSE analysis of salt decomposition rate for ode15s and sundialsTB.

C-rate	RMSE ($A.m^{-2}$)	
	CSM with ode15s	CSM with sundialsTB
0.1	0.0042	0.0034
0.2	0.0033	0.003
0.4	0.0036	0.0031
0.6	0.0034	0.003
0.8	0.0032	0.0026
1	0.0042	0.0039
2	0.0047	0.0041
3	0.0031	0.0026
5	0.0005	0.00041

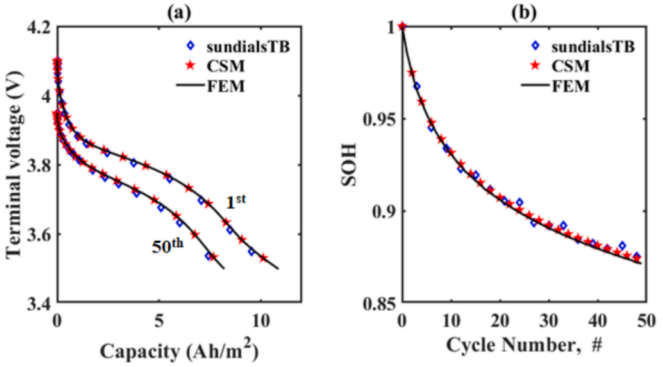

Fig. 4. Model prediction of capacity fade for an applied constant current of 1C. (a) Discharge curves at 1st and 50th cycles, (b) SOH evolution from 1st to 50th cycle.

Furthermore, to enhance model convergence and accuracy, the numerical Jacobian matrix for the DAE system is evaluated using

$$J=\begin{bmatrix}\frac{\partial f_1}{\partial y_1} & \frac{\partial f_1}{\partial y_2} & \cdots\\ \frac{\partial f_2}{\partial y_1} & \frac{\partial f_2}{\partial y_2} & \cdots\\ \vdots & \vdots & \end{bmatrix}. \tag{56}$$

Application of Eq. (56) to the DAE system given in Eq. (47) gives the following expression for the Jacobian matrix

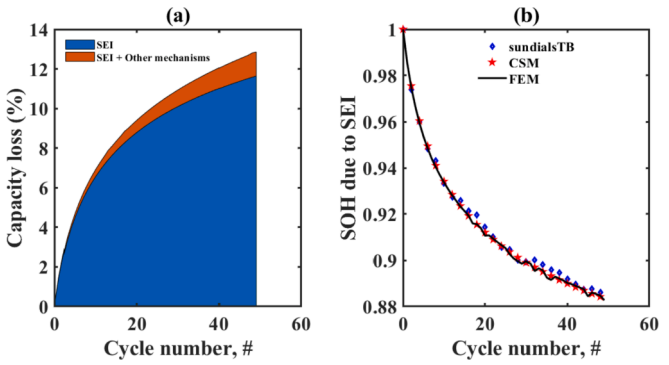

Fig. 5. Comparison of capacity loss due to specific degradation mechanisms (a) SEI growth and the other degradation mechanisms (Mn^{2+} deposition, H^{+} evolution, salt decomposition, Mn^{2+} dissolution and electrolyte oxidation) and (b) SOH due to only SEI growth.

3. Results

As earlier indicated, the capacity fade model employs a lithium manganese oxide ($Li_yMn_2O_4$) cathode and a graphite anode. The detailed parameters for this battery chemistry are given in Table 1. In addition, the requisite open circuit potential and electrolyte phase ionic conductivity expressions for the model are given in Appendix B. In order to verify the accuracy of the CSM capacity fade model in MATLAB®, this study's results were compared to that of a high-fidelity implementation of the model in COMSOL Multiphysics®. The high-fidelity model employs FEM, where the governing equations were implemented using the equation-based modeling toolbox. In both models (i.e., COMSOL Multiphysics® and CSM in MATLAB®), the second-order backward differentiation formula for time integration was employed. For additional computational validation purposes, the CSM capacity fade model was further implemented using the implicit-differential algebraic equation (IDAS) solver with sensitivity analysis capabilities in sundialsTB [34,35]. The sundialsTB code is a MATLAB interface to SUNDIALS (SUite of Nonlinear and Differential/Algebraic equation Solvers). All the capacity fade model simulations are implemented on a Windows 10 desktop (Intel Xeon 2.4 GHz 2 × processors) with an installed memory of 32 GB.

In the first simulation study, the voltage response as a function of C-rate (The terminology "C-rate" is defined as the measure of current flowing through a battery cell relative to its nominal capacity. In a simpler term, at 1C rate, a 17.5Ah cell should be able to deliver 17.5A for 1 h) for CSM with ode15s, CSM with sundialsTB and, FEM is considered. For CSM using ode15s and sundialsTB solvers, 10 Gauss-Lobatto nodes in each domain (i.e., anode, separator, and cathode) were employed, and twice that number were used in the radial direction. For the FEM model in COMSOL Multiphysics®, a fine mesh was used in the spatial direction. In all the models (CSM with ode15s, CSM with sundialsTB, and FEM), a relative tolerance of $\varepsilon = 10^{-6}$ was used. Also, for CSM with ode15s and FEM Multiphysics solvers, a second-order backward differentiation formula (BDF) is employed for time integration. Similarly, for the IDAS solver in sundialsTB, the variable-order, variable-coefficient backward differentiation formula [34] is utilized. In the results shown in Fig. 3a, the voltage curves for CSM using ode15s and sundialsTB solvers are compared to the high-fidelity FEM reference in COMSOL Multiphysics®. The root-mean-square-error (RMSE) values for the solvers relative to different C-rates are listed in Table 2. In the results, it is noticed that the RMSE values increase relative to C-rates. This trend is a by-product of the higher concentration and potential gradients associated with increasing C-rates, which in turn increases the degree of nonlinearity of the source terms. The RMSE change rate with respect to C-rate for ode15s and sundialsTB increased at a rate of 2.3062×10^{-4} /C and 7.8176×10^{-4} /C respectively. This result suggests that CSM using ode15s is slightly more accurate than sundialsTB.

Furthermore, the evolution of SEI layer thickness at the interface between the anode and separator (i.e., at x $= L_a$) in the first cycle is monitored. In Fig. 3b, the SEI layer grows parabolically, which is

Table 5
Voltage RMSE values for extended battery cycling (over 50 cycles).

C-rate	RMSE (mV)	
	CSM with ode15s	CSM with sundialsTB
0.1	77.0292	93.2302
0.2	30.689	54.6848
0.4	80.6012	158.6974
0.6	122.8533	226.0313
0.8	167.2253	211.6516
1	212.6184	238.1927

Table 6
SEI layer RMSE values for extended battery cycling (over 50 cycles).

C-rate	RMSE (nm)	
	CSM with ode15s	CSM with sundialsTB
0.1	0.0695	0.1702
0.2	0.02571	0.6041
0.4	0.1658	2.2558
0.6	0.3215	4.0017
0.8	0.4644	5.3863
1	0.6136	6.1147

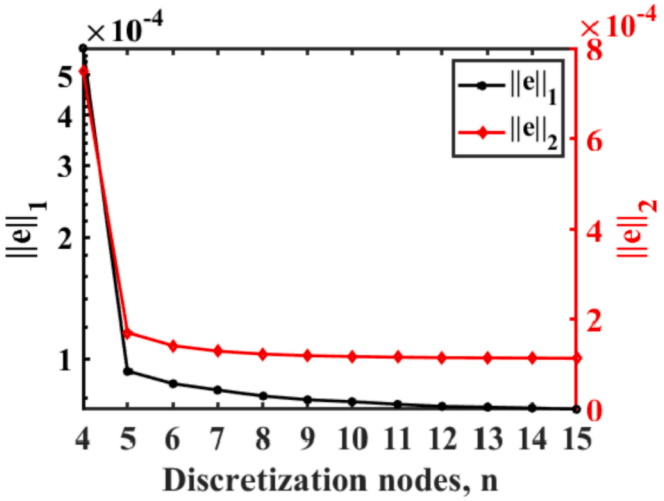

Fig. 6. CSM convergence rate with respect to discretization nodes.

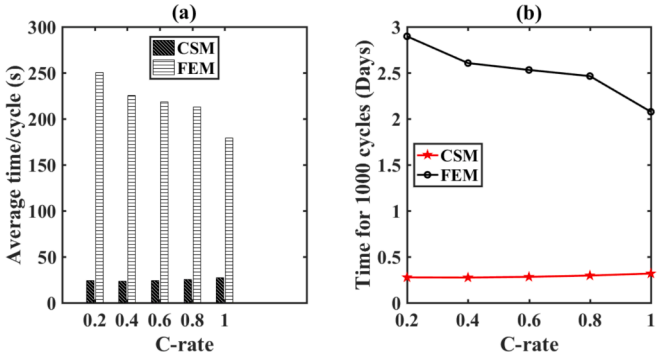

Fig. 7. Comparison of computation time using ode15s and FEM in COMSOL Multiphysics®. (a) Average simulation time per cycle. (b) Simulation time over 1000 cycles.

consistent with experimental results in the literature [36,37]. The SEI layer growth has been reported to have the most adverse effect on degradation in battery cells [20]. Its effect comes in the form of loss in cyclable lithium-ions and increase in cell resistance. In comparison with FEM, similar trends were noticed for the CSM using ode15s and the sundialsTB solver. The resulting SEI layer growth curves for CSM with ode15s and sundialsTB are closely matched with FEM (Fig. 3b). The RMSE values for the SEI layer thickness are computed and given in Table 3. Analysis of the values in Table 3, show a counterintuitive-relationship between RMSE and C-rate. The nature of the SEI growth curve, and the relationship between C-rate and time required to reach the cut-off voltage plays a role in this counterintuitive trend. The SEI layer curve, obeys the parabolic growth law which is rather uncomplicated especially in comparison with the voltage curves in Fig. 3a. At high C-rates, the expended time for reaching the prespecified cutoff voltage reduces, thereby precluding the accumulation of numerical errors, otherwise observed with low C-rates. For a complete picture of the underlying trend, a longer simulation run (treated further) accurately captures the relationship between SEI layer growth and C-rate.

The degradation mechanisms in the cathode electrode (i.e., Mn dissolution, electrolyte oxidation, and salt decomposition) lead to volume fraction changes. Reduction of the volume fraction in the cathode electrode adversely affects conductivity in the cathode electrode network. Fig. 3c shows the evolution of the electrode volume fraction at the interface between the cathode and current collector (i.e., $x = L_a + L_s + L_c$) for an applied current of 0.1C in the first cycle. Also, for the employed CSM and FEM discretization methods, a strong consistency between the solvers is observed. In addition, the evolution of salt decomposition rate at the interface between the cathode and current collector (i.e., at $x = L_a + L_s + L_c$) is analyzed. The salt decomposition rate has a direct impact on Mn dissolution. In the scenario where the cell terminal voltage supersedes the equilibrium potential for solvent oxidation (i.e., $U_{oxid}^{eq} = 4.1[V]$ in our model), the rate of salt decomposition increases rapidly, which in turn accelerates the formation of HF acid. The formed HF acid then directly attacks the $Li_yMn_2O_4$ active materials in the cathode electrode [21], which results in Mn dissolution. In the CSM and FEM results for salt decomposition rate in Fig. 3d, there is a good fit between the CSM and the high-fidelity FEM reference. In the RMSE analysis in Table 4, a counter-intuitive relationship between increasing C-rate and accuracy can be found. The reasons behind this trend, is consistent with the earlier discussion about the evolution of the SEI layer curve.

To analyze capacity fade using CSM, the impact of the degradation mechanisms on terminal voltage and state-of-health (SOH) for an applied current of 1C is shown in Fig. 4. In this figure, two terminal voltage curves for the 1st and 50th cycles are plotted. For the CSM using ode15s and sundialsTB, an adequately good fit relative to the high-fidelity FEM model in COMSOL Multiphysics® is observed. In the case of CSM using ode15s, a RMSE of 0.001358 is measured relative to FEM. Whereas in the case of CSM using the sundialsTB solver, the RMSE is found to be 0.0028. In both solvers, equal orders of accuracy in terms of RMSE is noticed, albeit CSM using ode15s seems to be slightly more accurate. As reported in [20], the degradation in a $Li_yMn_2O_4/Li_xC_6$ battery chemistry can be grouped sequentially into the acceleration, stabilization and saturation stages. In the acceleration stage, the impact of SEI layer formation is dominant where there is an active consumption of lithium-ions. In the stabilization stage, SEI growth slows down, and the loss of cyclable lithium-ions is reduced. In the final saturation stage, manganese dissolution is dominant and leads to active material losses. In Fig. 4b, the SOH changes due to all degradation mechanisms are shown. Furthermore, the specific contribution of SEI growth relative to the overall capacity fade in the model is analyzed. In the result shown in Fig. 5a, the overwhelming contribution of SEI to capacity loss in the model is observed, and this is quite consistent with reports in the literature [38]. For the SOH plot due to only SEI in Fig. 5b, there is a good fit between the reference FEM model and CSM. In the case of CSM using ode15s, the RMSE is found to be 0.00084, while that of CSM using sundialsTB is 0.002. This drop in order of accuracy with sundialsTB, is consistent with our previously reported results.

Additionally, the accuracy of the CSM models over extended cycling conditions is analyzed. For this, the models are implemented over 50 cycles with varying C-rates. The RMSE values for voltage and SEI, relative to the employed solvers are given in Table 5 and Table 6 respectively. In the case of voltage with ode15s, an order of magnitude decreases in accuracy from 0.4C to 0.6C is noticed. For sundialsTB, this same drop in accuracy is observed from 0.2C to 0.4C. In totality, the voltage RMSE values for ode15s and sundialsTB solvers over extended cycles increased at a rate of 3.228×10^{-2} /C and 3.6087×10^{-2} /C respectively. In the RMSE analysis of SEI growth, it is observed that ode15s and sundialsTB increased at a rate of 0.1198 /C and 1.309 /C respectively. In comparison, the RMSE values for the ode15s solver were consistently one order of magnitude less than that of sundialsTB.

The convergence rate of the CSM model using ode15s is analyzed in Fig. 6. Here, the model is implemented over a single cycle with varied number of discretization nodes. The corresponding accuracy is then measured using the base-10 logarithm of the norm expressions given in Appendix C. The numerical error values are characterized by a steep descent from $n = 4$ to $n = 5$, after which a continuous increase in the number of discretization nodes did not lead to significant improvement in accuracy. The general error (in terms of $log_{10}(\|e\|_1)$, $log_{10}(\|e\|_2)$) curve (or decay) are consistent with the expected exponential convergence [27] of the CSM. This is quite significant, in that with only a few additional discretization nodes, the accuracy of the approximation can be significantly improved.

To analyze the potential of the CSM model for real-time estimation, we examine the computation time using ode15s relative to the FEM model for 1000 cycles. A similar time comparison was not done for sundialsTB, because it is a MATLAB® interface to SUNDIALS solvers, which are originally written in ANSI C hence not ideal for time comparisons. In this analysis, the C-rates are varied, and the corresponding simulation times are plotted in Fig. 7. For example, the average simulation time at 0.2C is found to be about 10 times larger for FEM in COMSOL Multiphysics® compared to CSM using ode15s. In the FEM model in COMSOL Multiphysics®, a general decline in the simulation time with respect to C-rate is noticed. The reverse trend was observed for CSM. Here the simulation time was seen to increase per cycle relative to the increasing C-rates. This trend is due to the increasing potential and concentration gradients associated with higher C-rates. Furthermore, the re-initialization routine associated with the transition from charge to discharge cycles (and vice versa) also contributes to the increasing simulation time. This is because at the onset of the new cycling regime (charge or discharge), the BDF method employed by ode15s restarts; therefore, limiting the number of available prior timesteps, which adversely affects fast simulation time and convergence rate.

4. Summary and conclusions

This work represents the first attempt at an in-depth elucidation of the CSM in a comprehensive capacity fade model. This work applied the CSM method to implement an accurate, computationally efficient numerical model of the electrochemistry and fundamental degradation mechanisms in a battery system. Quasi-linearization techniques were applied to nonlinear source terms, which enhanced the convergence rate and led to the strengthening of the diagonal terms. Furthermore, a numerical Jacobian matrix using the CSM was derived, and it was found to enhance convergence and simulation time. Also, simulation studies were conducted for constant discharge cycles at various C-rates.

Implementation of the CSM for both ode15s and sundialsTB displayed good accuracy in comparison with the high-fidelity FEM model in COMSOL Multiphysics®. For example, in the case where ode15s is

implemented over 50 cycles at 1C, the accuracy was within 0.1358% of the reference FEM solver. In contrast, implementation of the CSM using sundialsTB showed results that were within 0.28% of the reference model. Although, both the ode15s and sundialsTB solvers employ a form of the BDF method for integration of the DAE system, it can be assumed that the differing integration platforms was responsible for the slight disparity in accuracy. In terms of computation time, a significant reduction using the CSM is observed. For example the analysis in Fig. 7 showed an average reduction in simulation time of approximately 91%. Future work will involve the use of an external algorithm (e.g., CasADi) for the derivation of an analytical Jacobian matrix, which has the potential to further improve accuracy and reduce simulation time.

Declaration of Competing Interest

The authors declare that they have no known competing financial interests or personal relationships that could have appeared to influence the work reported in this paper.

Acknowledgment

The authors gratefully acknowledge financial support from the National Science Foundation (Award Nos. 1610396 and 1917055).

Appendix A

Battery degradation equations

Mass conservation for Mn^{2+}

$$\varepsilon_{2,i}\cdot\frac{\partial c_{Mn^{2+}}}{\partial t}=D^{eff}_{Mn^{2+}}\frac{\partial^2 c_{Mn^{2+}}}{\partial x^2}+\frac{1}{F}i_{Mn\_dep},\qquad i=\quad a \tag{A.1}$$

$$\varepsilon_{2,i}\cdot\frac{\partial c_{Mn^{2+}}}{\partial t}=D^{eff}_{Mn^{2+}}\frac{\partial^2 c_{Mn^{2+}}}{\partial x^2},\qquad i=\quad s \tag{A.2}$$

$$\varepsilon_{2,i}\cdot\frac{\partial c_{Mn^{2+}}}{\partial t}=D^{eff}_{Mn^{2+}}\frac{\partial^2 c_{Mn^{2+}}}{\partial x^2}+\frac{a^{pos}_s}{F}i_{Mn\_dis},\qquad i=\quad c \tag{A.3}$$

$$D^{eff}_{Mn^{2+}}\left.\frac{\partial c_{Mn^{2+}}}{\partial x}\right|_{x=0}=0,\qquad D^{eff}_{Mn^{2+}}\left.\frac{\partial c_{Mn^{2+}}}{\partial x}\right|_{x=L_a+L_s+L_c}=0 \tag{A.4}$$

Mass conservation for H^+

$$\varepsilon_{2,i}\cdot\frac{\partial c_{H^+}}{\partial t}=D^{eff}_{H^+}\frac{\partial^2 c_{H^+}}{\partial x^2}+\frac{1}{F}j^{salt}_{H^+},\qquad i=\quad a,\quad s \tag{A.5}$$

$$\varepsilon_{2,i}\cdot\frac{\partial c_{H^+}}{\partial t}=D^{eff}_{H^+}\frac{\partial^2 c_{H^+}}{\partial x^2}+\frac{1}{F}\left(j^{oxid}_{H^+}\cdot a_c+j^{salt}_{H^+}-4\cdot a^{pos}_s i_{Mn\_react}\right),\qquad i=\quad c \tag{A.6}$$

$$k_{eff_a}\left.\frac{\partial c_{H^+}}{\partial x}\right|_{x=0}=0,\qquad k_{eff_c}\left.\frac{\partial c_{H^+}}{\partial x}\right|_{x=L_a+L_s+L_c}=0 \tag{A.7}$$

Mass conservation for H_2O

$$\varepsilon_{2,i}\cdot\frac{\partial c_{H_2O}}{\partial t}=D^{eff}_{H_2O}\frac{\partial^2 c_{H_2O}}{\partial x^2}-\frac{j^{salt}_{H^+}}{F},\qquad i=\quad a,s \tag{A.8}$$

$$\varepsilon_{2,i}\cdot\frac{\partial c_{H_2O}}{\partial t}=D^{eff}_{H_2O}\frac{\partial^2 c_{H_2O}}{\partial x^2}+\frac{1}{F}\left(2a^{pos}_s i_{Mn\_react}-j^{salt}_{H^+}\right)i_{Mn\_dis},\qquad i=\quad c \tag{A.9}$$

$$k_{eff_a}\left.\frac{\partial c_{H^+}}{\partial x}\right|_{x=0}=0,\qquad k_{eff_c}\left.\frac{\partial c_{H^+}}{\partial x}\right|_{x=L_a+L_s+L_c}=0 \tag{A.10}$$

Volume fraction of the solid phase (cathode)

$$\frac{\partial\varepsilon^{pos}_1}{\partial t}=-\frac{S_c\cdot i_{Mn\_react}\overline{V}}{F} \tag{A.11}$$

Usable volume fraction of the solid phase (cathode)

$$\frac{\partial\varepsilon^{pos}_{usable}}{\partial t}=-k_{iso}\frac{S_c\cdot i_{Mn\_react}\overline{V}}{F} \tag{A.12}$$

SEI film (anode)

$$\frac{d\delta_{SEI}}{dt}=\frac{-i_{SEI}M_{SEI}}{2F\rho_{SEI}} \tag{A.13}$$

SEI Resistance (anode)

$$R_{SEI}=k_{res}\cdot\delta_{SEI} \tag{A.14}$$

Auxiliary equations/side reactions

Butler-Volmer Equation (anode)

$$j_{loc,a} = i_0\left\{exp\left[\frac{\alpha_a F}{RT}\left(\eta_i - R_{SEI}\cdot j_{loc,a}\right)\right] - exp\left[\frac{-\alpha_c F}{RT}\left(\eta_i - R_{SEI}\cdot j_{loc,a}\right)\right]\right\} \tag{A.15}$$

Butler-Volmer equation (cathode)

$$j_{loc,c} = i_0\left\{exp\left[\frac{\alpha_a F}{RT}\eta_i\right] - exp\left[\frac{-\alpha_c F}{RT}\eta_i\right]\right\} \tag{A.16}$$

SEI current (anode)

$$i_{SEI} = -exp(-\lambda_{SEI}\cdot\delta_{SEI})\cdot F\cdot k_{SEI}\cdot c_{EC}\cdot exp\left(\frac{-\alpha_{SEI}F}{RT}(\varphi_1-\varphi_2)\right) \tag{A.17}$$

Mn deposition rate (anode)

$$i_{Mn\_dep} = -exp^{\left(-\lambda_{Mn\_dep}\cdot\delta_{SEI}\right)}F\cdot k_{Mn\_dep}\cdot c_{Mn^{2+}}\cdot exp\left(\frac{-\alpha_c^{Mn\_dep}2F}{RT}(\varphi_1-\varphi_2)\right) \tag{A.18}$$

Hydrogen evolution rate (anode)

$$i_{H_2} = -exp^{\left(-\lambda_{H_2}\cdot\delta_{SEI}\right)}F\cdot k_{H_2}\cdot c_{H^+}\cdot exp\left(\frac{-\alpha_c^{H_2}\cdot F}{RT}(\varphi_1-\varphi_2)\right) \tag{A.19}$$

Salt decomposition rate (anode, separator, cathode)

$$j_{H^+}^{salt} = F\cdot k_{decom}(c_{H_2O})^2 c_2 \tag{A.20}$$

Solvent oxidation rate (cathode)

$$j_{oxid} = i_0^{sol}\cdot exp\left(\frac{\alpha_a^{sol}F}{RT}\eta_{oxid}\right) \tag{A.21}$$

Mn dissolution rate (cathode)

$$i_{Mn\_dis} = f_{Mn\_dis}\underbrace{Fk_{dis}c_{H^+}}_{i_{Mn\_react}} \tag{A.22}$$

Solid phase concentration equation

$$\frac{\partial c_1}{\partial t} = D_{1,i}\frac{1}{r^2}\frac{\partial}{\partial r}\left(r^2\frac{\partial c_1}{\partial r}\right) \tag{A.23}$$

$$D_{1,i}\left.\frac{\partial c_1}{\partial r}\right|_{r=0} = 0 \tag{A.24}$$

$$D_{1,i}\left.\frac{\partial c_1}{\partial r}\right|_{r=R_a} = \frac{-j_{Li,i}}{F} \tag{A.25}$$

Solution phase concentration equation

$$\varepsilon_{2,i}\cdot\frac{\partial c_2}{\partial t} = D_i^{eff}\frac{\partial^2 c_2}{\partial x^2} + \frac{1-t^+}{F}S_i\cdot j_{loc,i} \qquad i = a \tag{A.26}$$

$$\varepsilon_{2,i}\cdot\frac{\partial c_2}{\partial t} = D_i^{eff}\frac{\partial^2 c_2}{\partial x^2}, \qquad i = s \tag{A.27}$$

$$\varepsilon_{2,i}\cdot\frac{\partial c_2}{\partial t} = D_i^{eff}\frac{\partial^2 c_2}{\partial x^2} + \frac{1-t^+}{F}S_i\cdot j_{loc,i} + \frac{(2S_i\cdot i_{Mn\_react} - j_{oxid}\cdot a_i)}{F}, \qquad i = c \tag{A.28}$$

Solid phase potential equation

$$\sigma_i^{eff}\frac{\partial^2\varphi_1}{\partial x^2} = S_i\cdot j_{loc,i} \tag{A.29}$$

$$\varphi_1|_{x=0} = 0 \tag{A.30}$$

$$\sigma_a^{eff}\left.\frac{\partial\varphi_1}{\partial x}\right|_{x=L_a} = \sigma_c^{eff}\left.\frac{\partial\varphi_1}{\partial x}\right|_{x=L_a+L_s} = 0 \tag{A.31}$$

$$\sigma_c^{eff}\left.\frac{\partial\varphi_1}{\partial x}\right|_{x=L_a+L_s+L_c} = -I_{app} \tag{A.32}$$

Solution phase potential equation

$$\frac{\partial}{\partial x}\left[-keff_i\left(\frac{\partial \varphi_2}{\partial x}-\frac{k_{junc}}{c_2}\frac{\partial c_2}{\partial x}\right)\right]=j_{loc,i}\cdot S_i \tag{A.33}$$

$$keff_a\left(\frac{\partial \varphi_2}{\partial x}-\frac{k_{junc}}{c_2}\frac{\partial c_2}{\partial x}\right)\Big|_{x=0}=keff_c\left(\frac{\partial \varphi_2}{\partial x}-\frac{k_{junc}}{c_2}\frac{\partial c_2}{\partial x}\right)\Big|_{x=L_a+L_s+L_c}=0 \tag{A.34}$$

Side-reaction coupling to the cell-level (anode)

$$j_{Li,a}=j_{loc,a}-i_{SEI}-i_{H_2}-i_{Mn\_dep} \tag{A.35}$$

Side-reaction coupling to the cell-level (cathode)

$$j_{Li,c}=j_{loc,c}+2\cdot i_{Mn\_react}-j_{oxid} \tag{A.36}$$

The continuity equations for the solution phase potential equation are:

$$\varphi_2|_{x=L_a^-}=\varphi_2|_{x=L_a^+} \tag{A.37}$$

$$keff_a\left(\frac{\partial \varphi_2}{\partial x}-\frac{k_{junc}}{c_2}\frac{\partial c_2}{\partial x}\right)\Big|_{x=L_a^-}=keff_s\left(\frac{\partial \varphi_2}{\partial x}-\frac{k_{junc}}{c_2}\frac{\partial c_2}{\partial x}\right)\Big|_{x=L_a^+} \tag{A.38}$$

$$\varphi_2|_{x=(L_a+L_s)^-}=\varphi_2|_{x=(L_a+L_s)^+} \tag{A.39}$$

$$keff_s\left(\frac{\partial \varphi_2}{\partial x}-\frac{k_{junc}}{c_2}\frac{\partial c_2}{\partial x}\right)\Big|_{x=(L_a+L_s)^-}=keff_c\left(\frac{\partial \varphi_2}{\partial x}-\frac{k_{junc}}{c_2}\frac{\partial c_2}{\partial x}\right)\Big|_{x=(L_a+L_s)^+} \tag{A.40}$$

In the case of the solution concentration equation, the continuity equations are,

$$c_2|_{x=L_a^-}=c_2|_{x=L_a^+} \tag{A.41}$$

$$D_a^{eff}\frac{\partial c_2}{\partial x}\Big|_{x=L_a^-}=D_s^{eff}\frac{\partial c_2}{\partial x}\Big|_{x=L_a^+} \tag{A.42}$$

$$c_2|_{x=(L_a+L_s)^-}=c_2|_{x=(L_a+L_s)^+} \tag{A.43}$$

$$D_s^{eff}\frac{\partial c_2}{\partial x}\Big|_{x=(L_a+L_s)^-}=D_c^{eff}\frac{\partial c_2}{\partial x}\Big|_{x=(L_a+L_s)^+} \tag{A.44}$$

The continuity equations for the evolving degradation species are given in Eqs. (A.45)–(A.56),

$$c_{Mn^{2+}}|_{x=L_a^-}=c_{Mn^{2+}}|_{x=L_a^+} \tag{A.45}$$

$$D_{Mn^{2+}}^{eff}\frac{\partial c_{Mn^{2+}}}{\partial x}\Big|_{x=L_a^-}=D_{Mn^{2+}}^{eff}\frac{\partial c_{Mn^{2+}}}{\partial x}\Big|_{x=L_a^+} \tag{A.46}$$

$$c_{Mn^{2+}}|_{x=(L_a+L_s)^-}=c_{Mn^{2+}}|_{x=(L_a+L_s)^+} \tag{A.47}$$

$$D_{Mn^{2+}}^{eff}\frac{\partial c_{Mn^{2+}}}{\partial x}\Big|_{x=(L_a+L_s)^-}=D_{Mn^{2+}}^{eff}\frac{\partial c_{Mn^{2+}}}{\partial x}\Big|_{x=(L_a+L_s)^+} \tag{A.48}$$

$$c_{H^+}|_{x=L_a^-}=c_{H^+}|_{x=L_a^+} \tag{A.49}$$

$$D_a^{eff}\frac{\partial c_{H^+}}{\partial x}\Big|_{x=L_a^-}=D_s^{eff}\frac{\partial c_{H^+}}{\partial x}\Big|_{x=L_a^+} \tag{A.50}$$

$$c_{H^+}|_{x=(L_a+L_s)^-}=c_{H^+}|_{x=(L_a+L_s)^+} \tag{A.51}$$

$$D_{H^+}^{eff}\frac{\partial c_{H^+}}{\partial x}\Big|_{x=(L_a+L_s)^-}=D_{H^+}^{eff}\frac{\partial c_{H^+}}{\partial x}\Big|_{x=(L_a+L_s)^+} \tag{A.52}$$

$$c_{H_2O}|_{x=L_a^-}=c_{H_2O}|_{x=L_a^+} \tag{A.53}$$

$$D_{H_2O}^{eff}\frac{\partial c_{H_2O}}{\partial x}\Big|_{x=L_a^-}=D_{H_2O}^{eff}\frac{\partial c_{H_2O}}{\partial x}\Big|_{x=L_a^+} \tag{A.54}$$

$$c_{H_2O}|_{x=(L_a+L_s)^-}=c_{H_2O}|_{x=(L_a+L_s)^+} \tag{A.55}$$

$$D_{H_2O}^{eff}\frac{\partial c_{H_2O}}{\partial x}\Big|_{x=(L_a+L_s)^-}=D_{H_2O}^{eff}\frac{\partial c_{H_2O}}{\partial x}\Big|_{x=(L_a+L_s)^+} \tag{A.56}$$

Appendix B

Open Circuit Potential Expression – Graphite [20]

$$U_{ocp}^{graphite} = -0.16 + 1.32 \cdot exp(-3 \cdot \theta) + 10 \cdot exp(-2000 \cdot \theta) \tag{B.1}$$

Open Circuit Potential Expression – $Li_yMn_2O_4$ [21,39]

$$\begin{aligned} U_{ocp}^{LMO} &= 4.19829 + 0.0565661 \cdot tanh(-14.5546 \cdot \theta + 8.60942) \\ &\quad -0.0275479 \cdot \left[\frac{1}{(0.998432 - \theta)^{0.492465}} - 1.90111 \right] \\ &\quad -0.157123 \cdot exp\left(-0.04738 \cdot \theta^{8}\right) + 0.810239 \cdot exp(-40 \cdot (\theta - 0.133875)) \end{aligned} \tag{B.2}$$

Electrolyte Phase Ionic Conductivity [20]

$$\begin{aligned} k_2 = {} & 6.1 \times 10^{-22} \cdot (c_2)^6 - 4.8 \times 10^{-18} \cdot (c_2)^5 + 2.1 \times 10^{-15} \cdot (c_2)^4 \\ & + 1.2 \times 10^{-10} \cdot (c_2)^3 - 5.2 \times 10^{-7} \cdot (c_2)^2 + 0.00068 \cdot c_2 + 0.0078 \end{aligned} \tag{B.3}$$

Appendix C

The norm expressions for error measurement are given as follows [40]:

$$\|e\|_1 = \frac{1}{N} \sum_{p=1}^{N} \left| U_{ref,FEM} - U_{CSM} \right| \tag{C.1}$$

$$\|e\|_2 = \left(\frac{1}{N} \sum_{p=1}^{N} \left| U_{ref,FEM} - U_{CSM} \right|^2 \right)^{\frac{1}{2}} \tag{C.2}$$

References

[1] A. Bizeray, S. Duncan, D. Howey, Advanced battery management systems using fast electrochemical modelling. IET Hybrid and Electric Vehicles Conference (HEVC), 2013.
[2] X. Lin, Y. Kim, S. Mohan, J.B. Siegel, A.G. Stefanopoulou, Modeling and estimation for advanced battery management, Annu. Rev. Control, Robotics, Autonomous Systems 2 (2019) 393–426.
[3] M.-K. Tran, A. DaCosta, A. Mevawalla, S. Panchal, M. Fowler, Comparative study of equivalent circuit models performance in four common lithium-ion batteries: LFP, NMC, LMO, NCA, Batteries 7 (3) (2021) 51.
[4] M.-K. Tran, M. Mathew, S. Janhunen, S. Panchal, K. Raahemifar, R. Fraser, M. Fowler, A comprehensive equivalent circuit model for lithium-ion batteries, incorporating the effects of state of health, state of charge, and temperature on model parameters, J. Storage Mater. 43 (2021), 103252.
[5] M.K. Tran, S. Panchal, V. Chauhan, N. Brahmbhatt, A. Mevawalla, R. Fraser, M. Fowler, Python-based scikit-learn machine learning models for thermal and electrical performance prediction of high-capacity lithium-ion battery, Int. J. Energy Res. (2021).
[6] S. Panchal, M. Rashid, F. Long, M. Mathew, R. Fraser, M. Fowler, Degradation testing and modeling of 200 ah LiFePO 4 battery, SAE Technical Paper (2018).
[7] A. Bizeray, S. Duncan, D. Howey, Advanced battery management systems using fast electrochemical modelling, (2013).
[8] A.M. Bizeray, S. Zhao, S.R. Duncan, D.A. Howey, Lithium-ion battery thermal-electrochemical model-based state estimation using orthogonal collocation and a modified extended Kalman filter, J. Power Sources 296 (2015) 400–412.
[9] D.J. Docimo, M. Ghanaatpishe, M.J. Rothenberger, C.D. Rahn, H.I. Fathy, The Lithium-Ion Battery Modeling Challenge, Mech. Eng. Magazine Select Articles 136 (06) (2014) S7–S14.
[10] A.V. Randall, R.D. Perkins, X. Zhang, G.L. Plett, Controls oriented reduced order modeling of solid-electrolyte interphase layer growth, J. Power Sources 209 (2012) 282–288.
[11] K. Smith, C.-Y. Wang, Power and thermal characterization of a lithium-ion battery pack for hybrid-electric vehicles, J. Power Sources 160 (1) (2006) 662–673.
[12] S.K. Rahimian, S.C. Rayman, R.E. White, Maximizing the life of a lithium-ion cell by optimization of charging rates, J. Electrochem. Soc. 157 (12) (2010) A1302.
[13] X. Lin, W. Lu, A framework for optimization on battery cycle life, J. Electrochem. Soc. 165 (14) (2018) A3380–A3388.
[14] D.A. Howey, S.A. Roberts, V. Viswanathan, A. Mistry, M. Beuse, E. Khoo, S. C. DeCaluwe, Free radicals: making a case for battery modeling, Electrochem. Society Interface 29 (4) (2020) 30–34.
[15] N.A. Chaturvedi, R. Klein, J. Christensen, J. Ahmed, A. Kojic, Algorithms for advanced battery-management systems, IEEE Control Syst. 30 (3) (2010) 49–68.
[16] A. Jossen, V. Spath, H. Doring, J. Garche, Battery management systems (BMS) for increasing battery life time, 21st International Telecommunications Energy Conference. INTELEC'99 (Cat. No. 99CH37007), IEEE, 1999, p. 56.
[17] P.W. Northrop, V. Ramadesigan, S. De, V.R. Subramanian, Coordinate transformation, orthogonal collocation, model reformulation and simulation of electrochemical-thermal behavior of lithium-ion battery stacks, J. Electrochem. Soc. 158 (12) (2011) A1461–A1477.
[18] F.B. Planella, M. Sheikh, W.D. Widanage, Systematic derivation and validation of a reduced thermal-electrochemical model for lithium-ion batteries using asymptotic methods, Electrochim. Acta 388 (2021), 138524.
[19] D.M. Ajiboye, J.W. Kimball, R.G. Landers, J. Park, Computationally efficient battery model for microgrid applications using the Chebyshev spectral method, Comput. Chem. Eng. 153 (2021) 107420.
[20] X. Lin, J. Park, L. Liu, Y. Lee, A.M. Sastry, W. Lu, A comprehensive capacity fade model and analysis for Li-ion batteries, J. Electrochem. Soc. 160 (10) (2013) A1701–A1710.
[21] Y. Dai, L. Cai, R.E. White, Capacity fade model for spinel LiMn2O4 electrode, J. Electrochem. Soc. 160 (1) (2013) A182–A190.
[22] C. Liu, Y. Gao, L. Liu, Toward safe and rapid battery charging: design optimal fast charging strategies thorough a physics-based model considering lithium plating, Int. J. Energy Res. 45 (2) (2021) 2303–2320.
[23] P. Ramadass, B. Haran, P.M. Gomadam, R. White, B.N. Popov, Development of first principles capacity fade model for Li-ion cells, J. Electrochem. Soc. 151 (2) (2004) A196–A203.
[24] A. Du Pasquier, A. Blyr, P. Courjal, D. Larcher, G. Amatucci, B. Gerand, J.M. Tarascon, Mechanism for Limited 55 C Storage Performance of Li1. 05Mn1. 95 O 4 Electrodes, Journal of The Electrochemical Society 146(2) (1999) 428-436.
[25] G. Zhou, X. Sun, Q.-H. Li, X. Wang, J.-N. Zhang, W. Yang, X. Yu, R. Xiao, H. Li, Mn Ion Dissolution Mechanism for Lithium-Ion Battery with LiMn2O4 cathode: in situ ultraviolet-visible spectroscopy and ab initio molecular dynamics simulations, J. Phys. Chem. Lett. 11 (8) (2020) 3051–3057.
[26] J.P. Boyd, Chebyshev and Fourier spectral methods, Courier Corporation (2001).
[27] L.N. Trefethen, Spectral methods in MATLAB, SIAM2000.
[28] W. Guo, G. Labrosse, R. Narayanan, The application of the Chebyshev-spectral method in transport phenomena, Springer Science & Business Media, 2013.
[29] S. Mazumder, Numerical methods for partial differential equations: finite difference and finite, Academic Press, 2015.
[30] L.N. Trefethen, Approximation Theory and Approximation Practice, Extended Edition, SIAM2019.
[31] M.T. Lawder, V. Ramadesigan, B. Suthar, V.R. Subramanian, Extending explicit and linearly implicit ODE solvers for index-1 DAEs, Comput. Chem. Eng. 82 (2015) 283–292.
[32] S. Patankar, Numerical Heat Transfer and Fluid Flow, Taylor & Francis, 2018.

[33] J.C. Forman, S. Bashash, J.L. Stein, H.K. Fathy, Reduction of an electrochemistry-based li-ion battery model via quasi-linearization and pade approximation, J. Electrochem. Soc. 158 (2) (2010) A93.
[34] A.C. Hindmarsh, P.N. Brown, K.E. Grant, S.L. Lee, R. Serban, D.E. Shumaker, C. S. Woodward, SUNDIALS: Suite of nonlinear and differential/algebraic equation solvers, ACM Trans. Mathematical Software (TOMS) 31 (3) (2005) 363–396.
[35] R. Serban, sundialsTB v2. 4.0, a matlab Interface to sundials, Technical Report2009.
[36] A.J. Smith, J.C. Burns, X. Zhao, D. Xiong, J.R. Dahn, A high precision coulometry study of the SEI growth in Li/graphite cells, J. Electrochem. Soc. 158 (5) (2011) A447.
[37] P.M. Attia, W.C. Chueh, S.J. Harris, Revisiting the t 0.5 Dependence of SEI Growth, J. Electrochem. Soc. 167 (9) (2020) 090535.
[38] X.-G. Yang, Y. Leng, G. Zhang, S. Ge, C.-Y. Wang, Modeling of lithium plating induced aging of lithium-ion batteries: Transition from linear to nonlinear aging, J. Power Sources 360 (2017) 28–40.
[39] Y. Dai, L. Cai, R.E. White, Simulation and analysis of stress in a Li-ion battery with a blended LiMn 2 O 4 and LiNi 0.8 Co 0.15 Al 0.05 O 2 cathode, J. Power Sources 247 (2014) 365–376.
[40] W.L. Oberkampf, C.J. Roy, Verification and Validation in Scientific Computing, Cambridge University Press, 2010.